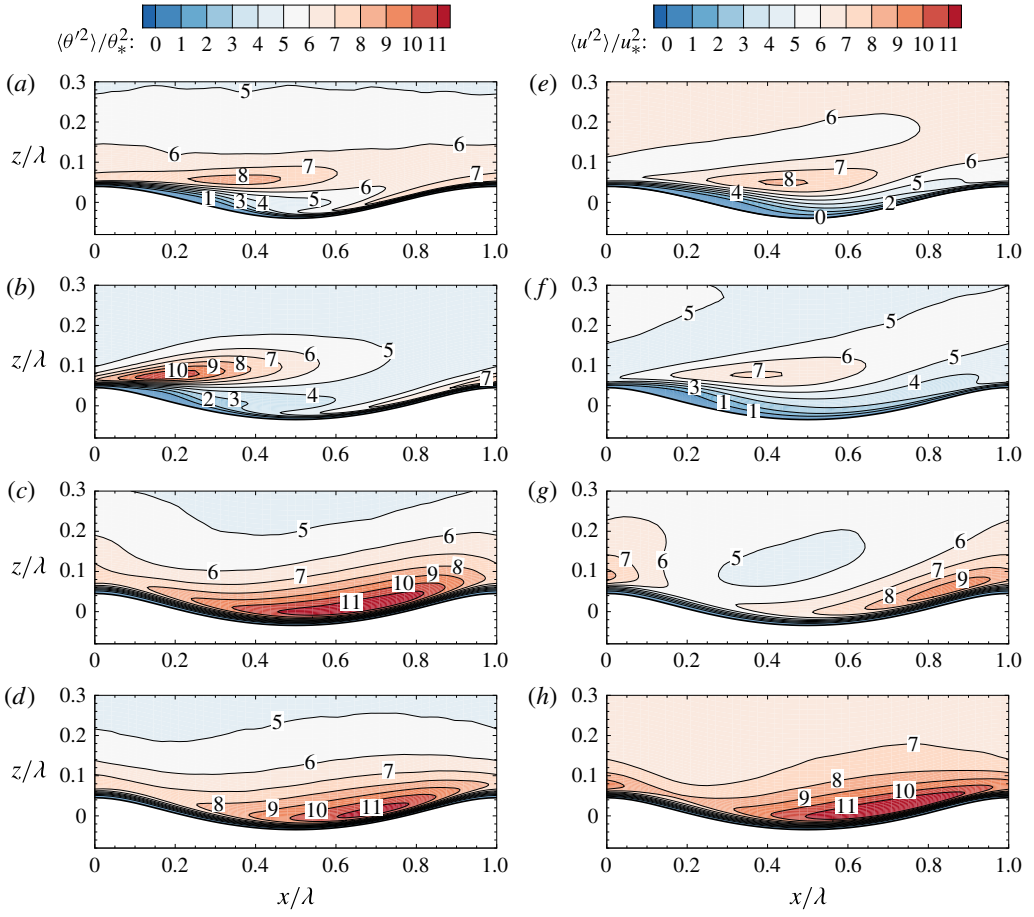

FIGURE 17. (Colour online) Contours of $\langle\theta'^2\rangle/\theta_*^2$ for various wave cases: (*a*) S25; (*b*) W25C2; (*c*) W25C14; and (*d*) W25C25. Contours of $\langle u'^2\rangle/u_*^2$ for various wave cases: (*e*) S25; (*f*) W25C2; (*g*) W25C14; and (*h*) W25C25. $Sc = 1.0$.

In particular, for each wave case the DNS results for $Sc = 1.0$ are presented. The results for other Schmidt numbers exhibit similar wave-correlated behaviours, and are thus not shown here.

Figure 17 shows the contours of the phase-averaged scalar variance, $\langle\theta'^2\rangle$, and the phase-averaged streamwise velocity variance, $\langle u'^2\rangle$. The scalar variance $\langle\theta'^2\rangle$ shows considerable correlation with $\langle u'^2\rangle$, and exhibits strong phase-dependent variation induced by the surface waves. In particular, for the stationary wave case S25 (figure 17*a*,*e*) there exists a strong shear layer with high intensity for $\langle\theta'^2\rangle$ and $\langle u'^2\rangle$, which originates from the crest and extends downstream to above the succeeding trough. In case W25C2 (figure 17*b*), the high-$\langle\theta'^2\rangle$ region is also located above the trough, but the maximum is located more upstream than that in case S25. The high-$\langle\theta'^2\rangle$ regions in cases S25 and W25C2 are consistent with the high vertical gradient regions for $\langle\theta\rangle$ shown in figures 3(*b*) and 3(*d*), respectively.

Different from cases S25 and W25C2, in cases W25C14 and W25C25 the high-$\langle\theta'^2\rangle$ regions are located above the windward face of the wave crest, and are much closer to the surface as a result of the smooth streamlines and $\langle\theta\rangle$ contour lines that are parallel

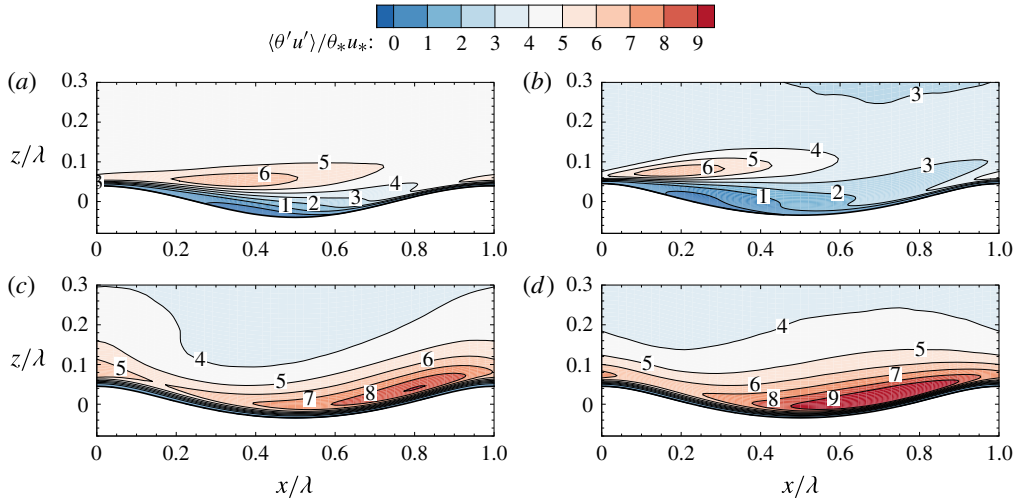

FIGURE 18. (Colour online) Contours of $\langle\theta' u'\rangle/\theta_* u_*$ for $Sc = 1.0$ and for various wave cases: (*a*) S25; (*b*) W25C2; (*c*) W25C14; and (*d*) W25C25.

to the wave surface in these two faster wave cases (figure 3*e–h*). The streamwise velocity variances $\langle u'^2\rangle$ for cases W25C14 (figure 17*g*) and W25C25 (figure 17*h*) show similar wave-correlated distributions as the corresponding $\langle\theta'^2\rangle$.

Consistent with the similarity between the $\langle\theta'^2\rangle$ and $\langle u'^2\rangle$ distributions, the horizontal scalar flux $\langle\theta' u'\rangle$ shown in figure 18 exhibits a similar wave-correlated distribution and wave condition dependence as in $\langle\theta'^2\rangle$ (cf. figure 17). Moreover, the wave-induced variations of $\langle\theta'^2\rangle$ and $\langle\theta' u'\rangle$ are mainly within the viscous wall region $\overline{z}^+ < 50$ (corresponding to $(z-\eta)/\lambda < 0.12$), consistent with the wave-affected region of the time- and plane-averaged profiles $\overline{\theta'}^+_{rms}$ and $\overline{\theta' u'}^+$ shown in figure 15.

Figure 19 shows the contours of the vertical scalar flux $\langle -\theta' w'\rangle$. Similar to $\langle\theta'^2\rangle$ and $\langle u'^2\rangle$, the presence of surface waves also induces significant wave-correlated variation in $\langle -\theta' w'\rangle$. In cases S25 and W25C2, the maximum $\langle -\theta' w'\rangle$ is located above the trough, in a region close to the region of maximum $\langle u'^2\rangle$ (cf. figure 17*e*,*f*). In cases W25C14 and W25C25, the maximum $\langle -\theta' w'\rangle$ is located above the leeward face of the crest. Moreover, there exists a distinct negative $\langle -\theta' w'\rangle$ region above the windward face of the crest, which does not exist in flat-wall boundary layer turbulence. The negative $\langle -\theta' w'\rangle$ region is insignificant in cases S25 and W25C2, but is prominent in cases W25C14 and W25C25. The distinct wave-induced negative $\langle -\theta' w'\rangle$ region near the windward face causes the time and plane average of $\overline{-\theta' w'}^+$ in the viscous sublayer to be significantly lower than that above a flat surface, as shown in figures 15(*f*) and 16(*f*).

A similar distinct negative vertical flux region was found for the Reynolds stress $\langle -u' w'\rangle$ in turbulence over intermediate and fast waves in the DNS studies by Yang & Shen (2009, 2010). Recently, the existence of the negative $\langle -u' w'\rangle$ region has also been observed in the laboratory experiment of Buckley & Veron (2016) using the particle image velocimetry technique. Yang & Shen (2009) studied the characteristics of coherent vortical structures in turbulence over progressive surface waves, and suggested that the significant negative Reynolds stress above the windward face is caused by the vertically bent quasi-streamwise vorticies. A similar mechanism is expected for generating the negative $\langle -\theta' w'\rangle$, which is studied in more detail in § 4.6.

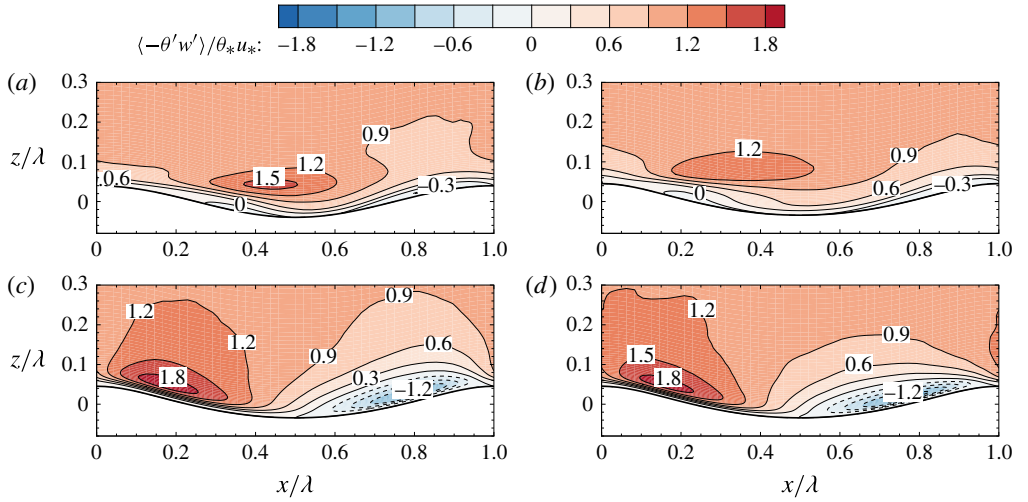

FIGURE 19. (Colour online) Contours of $\langle -\theta' w' \rangle / \theta_* u_*$ for $Sc = 1.0$ and for various wave cases: (*a*) S25; (*b*) W25C2; (*c*) W25C14; and (*d*) W25C25.

4.6. *Correlation between scalar and vortical structures*

Coherent vortical structures in turbulent boundary layer play an important role in the mixing and transport of momentum as well as scalars (e.g. Robinson 1991; Kawamura *et al.* 1998; Zedler & Street 2001; Choi & Suzuki 2005; Wallace 2016). In this subsection, the correlation between vortical structures and scalar fluctuations and fluxes is studied by direct observation of instantaneous vortices and the scalar field, and by conditional averages.

Figure 20 shows the instantaneous vortical structures and scalar fluctuations in the slow wave case W25C2. In particular, the vortices are visualized using the λ_2 method (Jeong & Hussain 1995). Based on the DNS data, the strain-rate tensor $\boldsymbol{S}$ and the rotation tensor $\boldsymbol{\Omega}$ are calculated, and λ_2 is the second largest eigenvalue of the tensor $\boldsymbol{S}^2 + \boldsymbol{\Omega}^2$. In the flow field, the regions with $\lambda_2 < 0$ correspond to the interior of vortices (Jeong & Hussain 1995). Moreover, in figure 20(*a*) the instantaneous vortices are coloured based on the streamwise vorticity, i.e. white if $\omega_x > 0$ and black if $\omega_x < 0$. In figure 20(*a*), several characteristic instantaneous vortices can be observed: reversed horseshoe vortices A and B, and quasi-streamwise vortices C–E. In particular, these reversed horseshoe vortices have their heads upstream and the two legs extended downstream, with $\omega_x > 0$ for the left leg and $\omega_x < 0$ for the right leg (observed when facing the $+x$-direction).

The correlation between these characteristic vortices and the scalar fluctuations can be clearly seen in figure 20(*b*,*c*). The reversed horseshoe vortices A and B are located above the wave trough. Taking vortex B as an example, the rotating motions of its head and two legs induce strong sweep motion ($w' < 0$) towards the wave trough and bring high θ downwards, resulting in $\theta' > 0$ and $-\theta' w' > 0$ (figure 20*b*). The effect of the reversed horseshoe vortex A on the scalar transport is similar to that of vortex B. Vortices C and D appear as a counter-rotating pair, and induce an upwelling motion (i.e. $w' > 0$) between them. Because on average θ increases with height, the upwelling flow ejects low θ upwards and generates a region of $\theta' < 0$; the combination of $w' > 0$ and $\theta' < 0$ results in a region with $-\theta' w' > 0$ between vortices C and D (figure 20*c*).

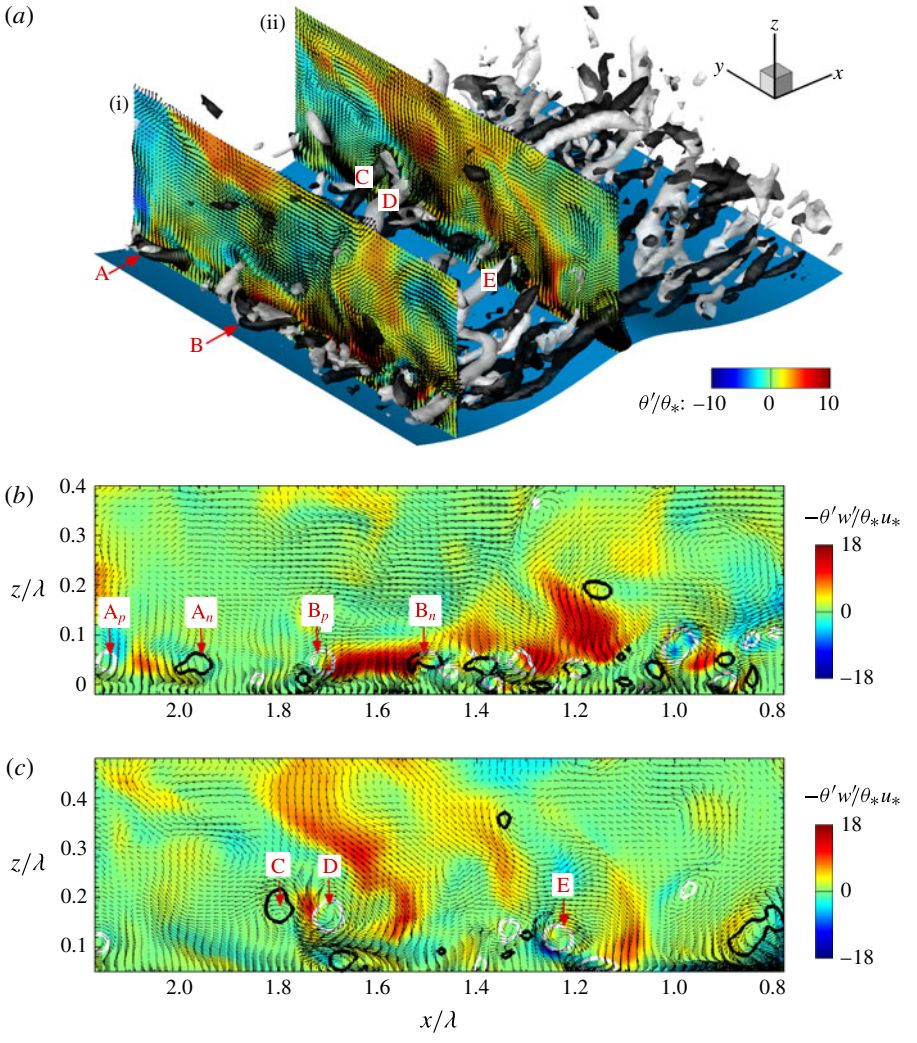

FIGURE 20. (Colour online) Instantaneous flow and scalar fields in turbulence over the slow wave (case W25C2, $Sc = 1.0$). Here only a small portion of the simulation domain is shown for illustration purposes. In (*a*), five characteristic vortices are marked, i.e. the reversed horseshoe vortices A and B and the quasi-streamwise vortices C–E. Two (y, z)-planes at the leeward face (plane i) and crest (plane ii) are plotted, with the contours of θ'/θ_* and vectors of (v', w') shown simultaneously. Zoom-in views of planes (i) and (ii) are plotted with the contours of $-\theta' w'/\theta_* u_*$ shown in (*b*) and (*c*), respectively. The instantaneous vortices are identified by the iso-surface of $\lambda_2 = -0.02$, with white colour for $\omega_x > 0$ and black colour for $\omega_x < 0$. In (*b*), the leg of vortex A with $\omega_x > 0$ is labelled as A_p, and the one with $\omega_x < 0$ is labelled as A_n. Similar notations are used to mark the two legs of vortex B.

The single quasi-streamwise vortex E generates a downwelling event ($w' < 0$) on its right side that brings high θ downwards and results in $\theta' > 0$ and $-\theta' w' > 0$ there.

The above correlations between the vortices and scalar fluctuations in the slow wave case are similar to those in turbulence over flat boundaries (see the reviews

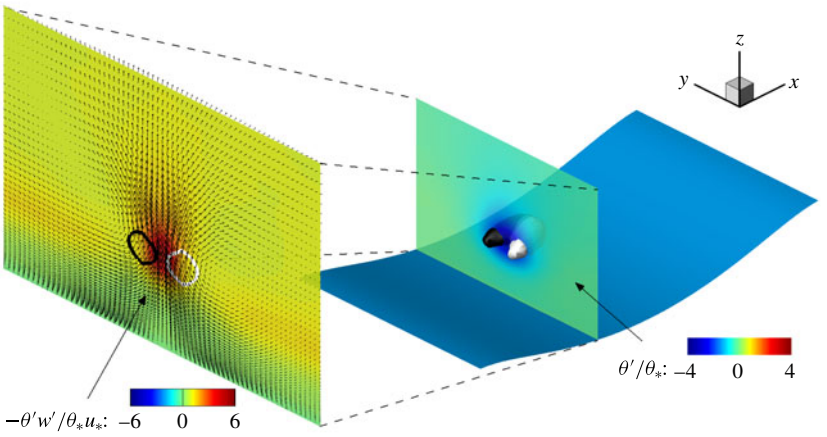

FIGURE 21. (Colour online) Educed flow and scalar fields for case W25C2 with $Sc = 1.0$ by conditional average of the Q2 events above the wave trough. The horseshoe vortex is visualized by the iso-surfaces of $\lambda_2 = -0.002$, with white colour on the leg with $\omega_x > 0$ and black colour on the leg with $\omega_x < 0$. Contours of θ'/θ_* are shown on the vertical plane across the two legs. Contours of $-\theta'w'/\theta_*u_*$ and vectors of (v', w') are shown in the zoom-in view of the vertical plane, on which the thick white and black lines are the iso-contour lines of $\lambda_2 = -0.002$.

by Robinson 1991; Wallace 2016). As shown by the statistical analysis in Yang & Shen (2009, 2010), in turbulence over progressive surface waves, different types of characteristic vortices are present for different wave conditions, and these different characteristic vortices also have different preferential locations relative to the surface waves. In the case of slow waves, reversed horseshoe vortices are usually generated above the wave trough, and then break up into quasi-streamwise vortices as their legs are stretched downstream (Yang & Shen 2009). Then the quasi-streamwise vortices are convected downstream and lifted upwards over the succeeding wave crests and troughs. The combination of the wave-phase-dependent distribution of the coherent vortices and their strong correlations with the scalar fluctuations provides a mechanism for generating the wave-correlated distributions of the scalar variance $\langle\theta'^2\rangle$ (figure 17) and the scalar fluxes $\langle\theta'u'\rangle$ (figure 18) and $\langle-\theta'w'\rangle$ (figure 19).

The correlation between vortices and scalar fluctuations can be further investigated by a conditional average based on the quadrants of the vertical turbulent flux (Wallace 2016). Similar to the quadrant analysis for Reynolds stress, the vertical scalar flux $\langle-\theta'w'\rangle$ can be divided into four quadrants based on the signs of θ' and w': Q1 ($\theta' > 0$, $w' > 0$), Q2 ($\theta' < 0$, $w' > 0$), Q3 ($\theta' < 0$, $w' < 0$) and Q4 ($\theta' > 0$, $w' < 0$). The coherent flow structure related to a specific quadrant can be educed by conditionally sampling and averaging the instantaneous flow events of the chosen quadrant. A brief introduction to the quadrant conditional average scheme used in the current analysis is given in appendix C.

For case W25C2, quadrant analysis indicates that the strong vertical scalar flux above the wave trough shown in figure 19(*b*) is mainly due to the Q2 and Q4 events (see figure 30). By applying the quadrant-based conditional average above the wave trough, the coherent flow structures associated with the Q2 and Q4 events can be educed. Figure 21 shows that a horseshoe vortex (with its head on the downstream

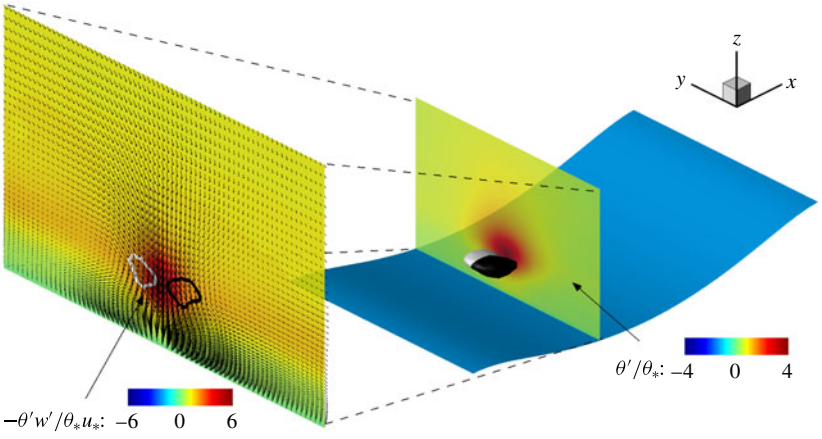

FIGURE 22. (Colour online) Educed flow and scalar fields for case W25C2 with $Sc = 1.0$ by conditional average of the Q4 events above the wave trough. The reversed horseshoe vortex is visualized by the iso-surface of $\lambda_2 = -0.0008$, with white colour on the leg with $\omega_x > 0$ and black colour on the leg with $\omega_x < 0$. Contours of θ'/θ_* are shown on the vertical plane across the two legs. Contours of $-\theta'w'/\theta_*u_*$ and vectors of (v', w') are shown in the zoom-in view of the vertical plane, on which the thick white and black lines are the iso-contour lines of $\lambda_2 = -0.0008$.

side) is educed by a conditional average of Q2 events above the wave trough. Such a vortex induces ejection of lower θ upwards (since θ has lower value near the bottom boundary), which results in $\theta' < 0$ and $-\theta'w' > 0$ between the two legs. It should be pointed out that direct observation of the instantaneous snapshots suggests the presence of quasi-streamwise vortices and horseshoe vortices (with the heads located downstream relative to the legs) in this flow region, both of which contribute to the Q2 events. Because the quadrant-based conditional average does not distinguish these two types of vortices, the educed flow field in figure 21 should account for the contribution of both types of vortices.

Figure 22 shows the conditionally averaged flow and scalar fields for Q4 events in case W25C2. The educed vortical structure exhibits a clear reversed horseshoe shape located slightly above the wave trough, which represents well the instantaneous reversed horseshoe vortices observed from the instantaneous snapshots (figure 20). The reversed horseshoe vortex induces downwelling motion that sweeps high θ towards the wave trough, which results in $\theta' > 0$ and $-\theta'w' > 0$ between the two legs. The reversed horseshoe vortex educed from Q4 events (figure 22) is located lower than the vortex pair educed from Q2 events (figure 21).

Different from the slow wave case discussed above, in the intermediate (W25C14) and fast (W25C25) wave cases the dominant flow structures are the vertically bent quasi-streamwise vortices, e.g. the vortices A–D shown in figure 23(*a*). Yang & Shen (2009) showed that the characteristics of coherent vortices in turbulence over intermediate and fast waves are very similar, with the difference mainly in the population and intensity of the vortices. Therefore, the analysis here focuses on the intermediate wave case W25C14 as a representative case. Figure 23 shows the instantaneous vortex and scalar fields in case W25C14, and figure 24 shows a sketch that illustrates the correlation between a vortex and the vertical scalar flux. In a

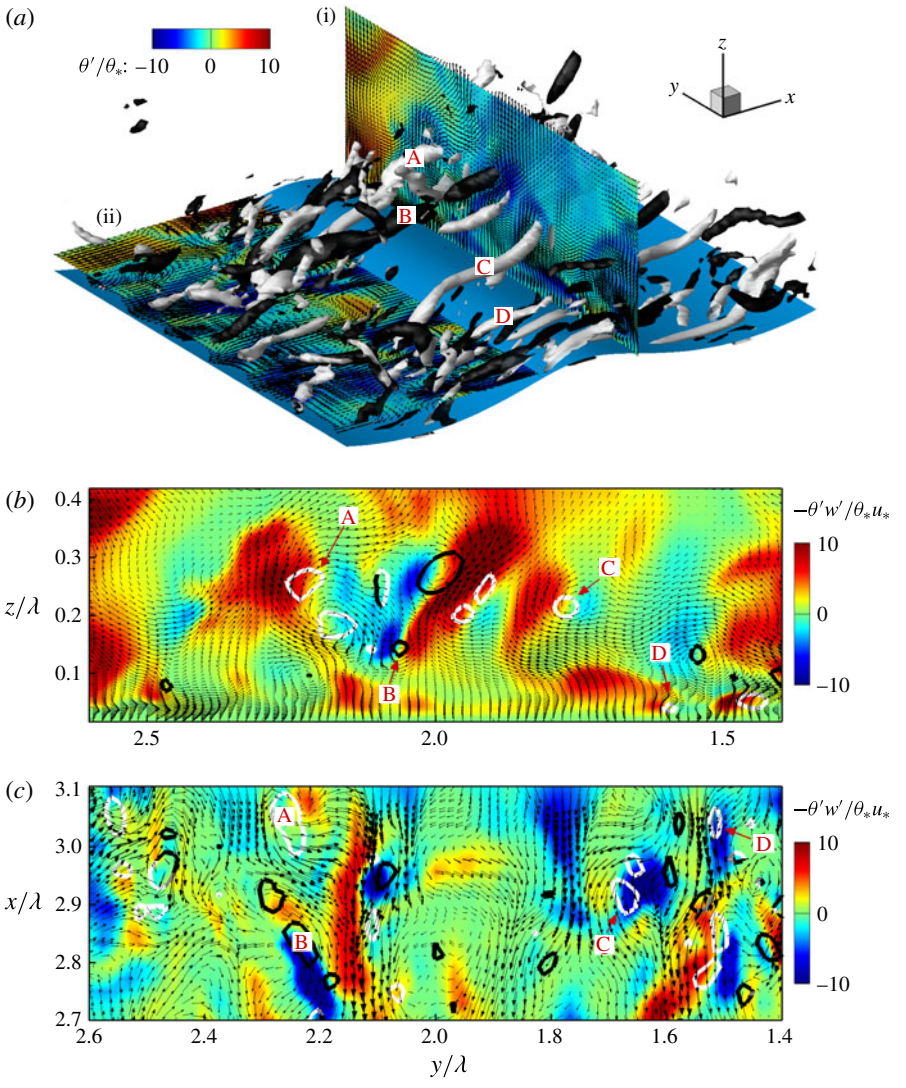

FIGURE 23. (Colour online) Instantaneous flow and scalar fields in turbulence over the intermediate wave (case W25C14, $Sc = 1.0$). Only a small portion of the simulation domain is shown for illustration purposes. Four characteristic vertically bent quasi-streamwise vortices (A–D) are marked. In (*a*), the instantaneous vortices are identified by the iso-surface of $\lambda_2 = -0.02$, with white colour for $\omega_x > 0$ and black colour for $\omega_x < 0$. The (y, z)-plane above the leeward face (plane i) and the (x, z)-plane above the windward face (plane ii) are plotted, with the contours of θ'/θ_* and vectors of velocity fluctuation (the components parallel to each plane) shown simultaneously. Panels (*b*) and (*c*) show the contours of the scalar flux $-\theta'w'/\theta_*u_*$ on planes (i) and (ii), respectively. In (*b*) and (*c*), the locations of the vortices are indicated by the iso-contours of $\lambda_2 = -0.02$, with white colour for $\omega_x > 0$ and black colour for $\omega_x < 0$.

reference frame moving at the wave phase speed, the near-surface vortices travel backwards in the $-x$-direction (see the mean streamlines shown in figure 3). They appear to be straight and horizontally oriented above the leeward face and the crest,

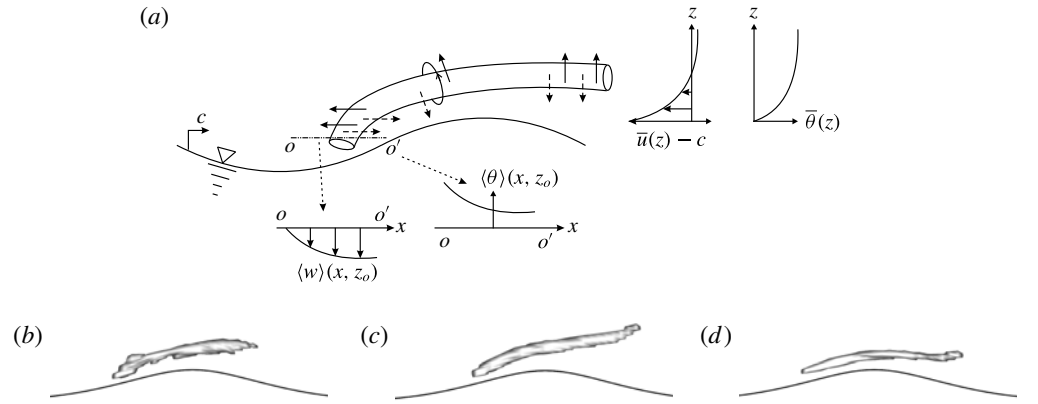

FIGURE 24. Sketch of the characteristic vortical structure (i.e. the vertically bent quasi-streamwise vortex) in turbulence over intermediate and fast waves. Panel (*a*) illustrates the correlation between the vortex and the turbulent fluctuations of velocity and scalar. The arrows near the vortex indicate the velocity fluctuation vectors associated with the vortex, with solid arrows in front of the vortex and dashed arrows behind the vortex. Panels (*b–d*) show three representative samples of the instantaneous vortices extracted from the DNS data of case W25C14.

and then bend downwards as they travel over the windward face. The unique shape and wave-phase correlation of the vortices result in the wave-correlated scalar flux shown in figure 19(*c*,*d*).

Taking the vortex C in figure 23 as an example, its horizontal part above the leeward face induces an upwelling motion (i.e. $w' > 0$) on its left side (observed when facing the $+x$-direction), which ejects low θ upwards and results in $\theta' < 0$ (see plane-i in figure 23*a*) and leads to a Q2 flux $-\theta' w' > 0$ (figure 23*b*). This mechanisms is similar to the Q2 flux generation mechanism in case W25C2. On the other hand, the vertical part of the vortex C above the windward face induces a horizontal velocity fluctuation $u' < 0$ on its left side (observed when facing the $+x$-direction), which induces a vertical velocity fluctuation $w' < 0$ because $\partial\langle w\rangle/\partial x < 0$ there (Yang & Shen 2009) (also see figure 3*e* and the sketch in figure 24*a*). Similarly, the fluctuation $u' < 0$ induces a scalar fluctuation of $\theta' < 0$ because $\partial\langle\theta\rangle/\partial x < 0$ there (figure 3*f* and the sketch in figure 24*a*). These correlations result in $\theta' u' > 0$ and $-\theta' w' < 0$ above the windward face of the wave crest, as shown in figures 18(*c*) and 19(*c*), respectively.

Similar to case W25C2, a quadrant-based conditional average can be done for case W25C14 to educe a statistical description of the correlation between vortical structures and scalar fluxes. As shown in figure 31 in the appendix C, in case W25C14 the positive vertical scalar flux $-\theta' w'$ above the leeward face is mainly due to the Q2 and Q4 events, while the negative vertical scalar flux above the windward face is mainly due to the Q1 and Q3 events. This result is consistent with the direct observation of the instantaneous flow and scalar fields shown in figure 23. Based on these wave-phase preferences, Q2 and Q4 events are conditionally sampled above the leeward face, and Q1 and Q3 events are conditionally sampled above the windward face. The specific locations where quadrant events detectors are applied are marked in figure 31.

Figure 25 shows the conditionally averaged Q2 event above the leeward face of case W25C14. Note that unlike in figures 21 and 22 where the vortices are visualized by

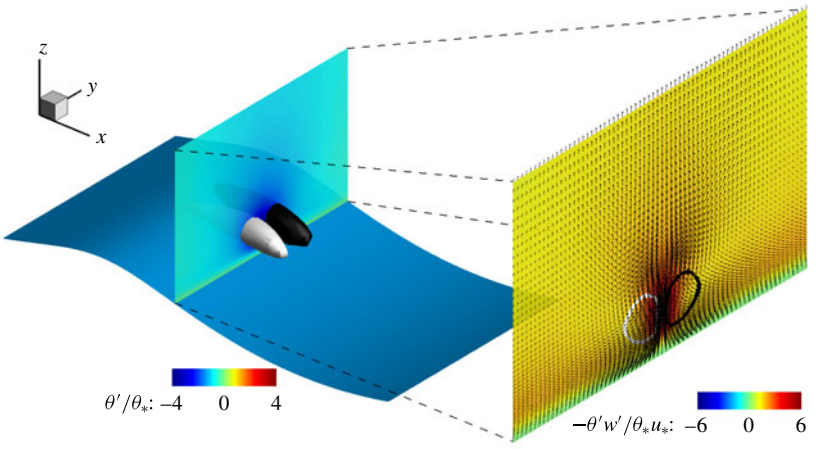

FIGURE 25. (Colour online) Educed flow and scalar fields for case W25C14 with $Sc = 1.0$ by conditional average of the Q2 events above the leeward face of the wave crest. The pair of vortices are visualized by the iso-surfaces of $|\omega_x/(u_*^2/\nu)| = 0.05$, with white colour for $\omega_x > 0$ and black colour $\omega_x < 0$. Contours of θ'/θ_* are shown on the vertical plane across the vortex pair. Contours of $-\theta' w'/\theta_* u_*$ and vectors of (v', w') are shown in the zoom-in view of the vertical plane, on which the thick white and black lines are the iso-contour lines of $\omega_x/(u_*^2/\nu) = 0.05$ and -0.05, respectively.

the λ_2 method, in figure 25 the vortices are visualized using the iso-surfaces of $|\omega_x|$. This is because in turbulence over intermediate and fast propagating surface waves (as well as in oscillating flow over stationary waves), the strong relative oscillation between the mean flow and the surface waves generates thin vortex sheets with significant spanwise vorticity in the vicinity of the wave crests and troughs (e.g. Tseng & Ferziger 2003; Yang & Balaras 2006; Yang & Shen 2009). In figure 23, those thin vortex sheets have been removed to provide a clear visualization of other coherent flow structures. However, because of their persistent presences at fixed wave phases (i.e. above crests and troughs), these vortex sheets also appear in the conditionally averaged field, with magnitudes larger than those of the vortices associated with the quadrant events. As a result, the desired vortices would not be clearly seen when the λ_2 method is used for visualization. Instead, the iso-surfaces of $|\omega_x|$ are good alternative for visualization because the horizontal part of a quasi-streamwise vortex above the leeward face in case W25C14 has a significant streamwise vorticity ω_x. Similarly, the iso-surfaces of $|\omega_z|$ are used for visualizing the vertical part of the vortex above the windward face. As shown in figure 25, the conditional average of Q2 events exhibits a pair of counter-rotating streamwise vortices above the leeward face, which induce upwelling motion ($w' > 0$) between them and result in $\theta' < 0$ and $-\theta' w' > 0$. Note that in figure 25 the vortices appear in pairs because the Q2 events generated by vortices with $\omega_x > 0$ and $\omega_x < 0$ are both sampled and included in the averaging process. In the instantaneous snapshots, these vortices usually appear individually.

A similar quadrant-based conditional average can be applied for all the four quadrants. Figure 26 shows the results for the four quadrants. Note that, as discussed above, in figure 26(*a*,*c*) the vortices are visualized using the iso-surfaces of $|\omega_z|$, while in figure 26(*b*,*d*) the vortices are visualized based on $|\omega_x|$. For all the four quadrants

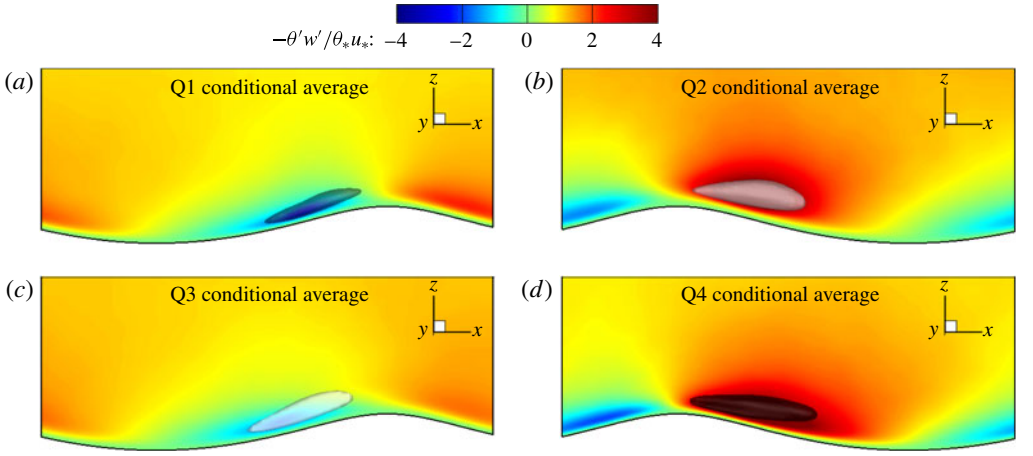

FIGURE 26. (Colour online) Side view of the educed flow and scalar fields for case W25C14 with $Sc = 1.0$ by conditional average based on the four different quadrants of $\langle -\theta'w' \rangle$: (*a*) Q1 ($\theta' > 0, w' > 0$) events above the windward face; (*b*) Q2 ($\theta' < 0, w' > 0$) events above the leeward face; (*c*) Q3 ($\theta' < 0, w' < 0$) events above the windward face; and (*d*) Q4 ($\theta' > 0, w' < 0$) events above the leeward face. In the figure, the colour contours are for $-\theta'w'/\theta_*u_*$ on the (x, z)-plane across the centre of the educed field. In each panel, the vortical structures are represented by the iso-surfaces of (*a*) $\omega_z/(u_*^2/\nu) = -0.05$, (*b*) $\omega_x/(u_*^2/\nu) = 0.05$, (*c*) $\omega_z/(u_*^2/\nu) = 0.05$, and (*d*) $\omega_x/(u_*^2/\nu) = -0.05$, respectively. In particular, light colour iso-surfaces correspond to positive vorticities (i.e. $\omega_x > 0$ or $\omega_z > 0$) and dark colour ones correspond to negative vorticities (i.e. $\omega_x < 0$ or $\omega_z < 0$).

the educed vortices appear in pair, but only the ones in front of the central (x, z)-plane of the averaged field are shown in figure 26. Both the conditionally averaged vortices and the scalar flux fields agree with the observation of the instantaneous snapshot in figure 23 and the phase-averaged scalar flux contours in figures 19(*c*) and 31.

It should be noted that the characteristics of the vortical structures may vary with the Reynolds number. The results presented in § 4.6 are based on DNS with a Reynolds number lower than that in a real marine wind condition. Therefore, caution should be taken when interpreting the vortical structures reported in this DNS study and linking them to those in the more realistic field condition. Nevertheless, the vortical structures found in the current DNS as well as their correlations with the distribution of scalar flux still provide useful insights for explaining the flow structures over progressive waves on a laboratory scale such as the recent experiment by Buckley & Veron (2016), in which they observed negative Reynolds stress above the windward face of air flow over fast propagating surface waves similar to the results obtained from the current DNS (see figures 19, 26 and 31).

5. Conclusions

Scalar transport in air turbulence over progressive surface waves plays an important role in air–sea interaction. The presence of progressive waves at the sea surface imposes great challenges to modelling the turbulent flow and scalar transport above the waves. To tackle this complex problem, in this study a wave boundary-fitted DNS turbulence solver previously developed by Yang & Shen (2011*a*) is employed, and is further expanded by including a scalar transport solver also based on the

boundary-fitted computational grid system. This expanded DNS model is shown to be able to capture the details of the complex scalar transport phenomena in the vicinity of the wave surface.

Using the DNS, the effects of surface wave motions on the scalar transport are studied in detail. In particular, three representative wave ages (i.e. the wave phase speed normalized by the wind friction velocity) are considered, representing the slow, intermediate and fast wave conditions, respectively. Statistical analyses of the DNS data show a strong wave phase dependence in the distributions of scalar concentration, scalar variance, turbulent scalar fluxes, and local Sherwood number along the wave surface. Comparison of the statistics among different wave conditions also reveals a significant effect of the wave age on the scalar transport.

The wave age effect is also pronounced in the time and plane average of these quantities, suggesting the importance of including the surface wave effect in models that cannot directly capture the wave-phase-induced disturbance. In particular, the vertical profiles of the time- and plane-averaged scalar for various wave conditions exhibit similar structures to those found in turbulence over a flat wall, i.e. a linear profile in the near-surface viscous sublayer ($\overline{z}^+ < 5$ in wall unit) and a logarithmic profile in the displaced log-law region ($50 < \overline{z}^+ < 150$). However, the von Kármán constant and the effective wave surface roughness for the mean scalar profile exhibit considerable variation with the wave age. The effect of the Schmidt number on the time and plane average of scalar is also quantified, which is found to be similar to that in flat-wall turbulence.

Moreover, the profiles of the root-mean-square scalar fluctuation and the horizontal scalar flux exhibit good scaling behaviours in the viscous sublayer that agree with the scaling laws previously reported for flat-wall turbulence, but considerable wave-induced variation is found in the viscous wall region above the sublayer ($5 < \overline{z}^+ < 50$). In addition, the profiles of the vertical scalar flux in the viscous sublayer over surface waves exhibit considerable discrepancies from the reported scaling law for the flat-wall turbulence. A close look at the two-dimensional contours of the phase-averaged vertical scalar flux indicates that the discrepancy is caused by a negative vertical flux region above the windward face of the wave crest, especially in the intermediate and fast wave cases.

Detailed analyses show that the instantaneous scalar fluctuations and fluxes are highly correlated with the coherent vortical structures in the turbulence above the wave surface, which exhibit clear wave-dependent characteristics in terms of their shapes and preferential locations. In particular, the characteristic vortices vary from quasi-streamwise (above windward face) and reversed horseshoe (above trough) shapes in the slow wave case, to vertically bent vortices over wave crests in the intermediate and fast wave cases. Direct observation of the instantaneous snapshots as well as quadrant-based conditional average analysis indicates that the wave age dependence of the wave-correlated scalar variance and flux distributions is caused by the combined effects of the characteristic vortices, their preferential locations, and the local gradient of the scalar concentration in the vicinity of these vortices.

It should be noted that in real open-sea conditions, the wind-generated waves usually have a broadband spectrum, with short waves steeper and propagating slower than long waves. Certain wave modes may also have an oblique angle relative to main wind direction. These effects are not considered in the current DNS study with a canonical configuration, and should be investigated in future studies.

Acknowledgements

D.Y. acknowledges financial support from his start-up funds as well as technical support from the Center for Advanced Computing and Data Systems (CACDS) and the Research Computing Center (RCC) at the University of Houston to carry out the simulations presented here. The support to L.S. through the ONR CASPER MURI project (N00014-16-1-3205) and the NSF award OCE-1341063 is gratefully acknowledged.

Appendix A. Validation with flat-wall case

To validate the DNS flow and scalar solvers, a series of test cases for turbulent Couette flows with a flat bottom boundary are performed. In particular, three different Reynolds numbers $Re_* = u_*\delta/\nu = 180$, 283, and 455 are considered, where δ is the half domain height. For each Reynolds number, four different Schmidt numbers, $Sc = 0.4$, 0.71, 1.0, and 3.0, are considered. These DNS results are compared with experimental and numerical results collected from the literature.

Figure 27 shows the profiles of mean streamwise velocity $\overline{u}^+$ and velocity fluctuation r.m.s. ($\overline{u'}^+_{rms}$, $\overline{v'}^+_{rms}$, $\overline{w'}^+_{rms}$). The current DNS results agree well with the experimental and DNS results in the literature for turbulent Couette flows and channel flows. In figure 27(*a*), the mean velocity profile obeys a linear law of $\overline{u}^+ = z^+$ in the viscous sublayer at $z^+ < 5$, and a logarithmic law of $\overline{u}^+ = (1/0.41)\ln(z^+) + 5.2$ in the log-law region at $z^+ > 30$. In figure 27(*b*), the velocity fluctuation r.m.s. exhibits anisotropy, with the magnitude of $\overline{u'}^+_{rms}$ larger than the other two components. Note that in turbulent Couette flow the vertical gradient of the mean velocity remains finite so that the velocity fluctuations reach a plateau towards the centre of the channel and remain anisotropic, while in a turbulent channel flow the streamwise velocity fluctuation r.m.s. magnitude reduces more significantly towards the centre of the channel (Debusschere & Rutland 2004). Therefore, in figure 27(*b*) only the results for turbulent Couette flows in the literature are plotted.

Figure 28 shows the profiles of mean scalar $\overline{\theta}^+$ and scalar fluctuation r.m.s. $\overline{\theta'}^+_{rms}$. Similar to the mean velocity, the profiles of $\overline{\theta}^+$ also exhibit a linear profile in the viscous sublayer and a logarithmic profile in the log-law region. The DNS results at different Re_* show only very small differences in $\overline{\theta}^+$. The change of Schmidt number has a more significant effect, with $\overline{\theta}^+$ increasing as Sc increases. By compiling a collection of experimental data, Kader (1981) found that the near-wall linear profile of the mean scalar follows

$$\overline{\theta}^+ = Sc\, z^+, \tag{A 1}$$

and the log-law profile follows

$$\overline{\theta}^+ = \frac{1}{\kappa_\theta}\ln(z^+) + B_\theta(Sc), \tag{A 2}$$

where $\kappa_\theta = 0.47$ and

$$B_\theta(Sc) = (3.84Sc^{1/3} - 1.3)^2 + 2.12\ln(Sc). \tag{A 3}$$

As shown in figure 28(*a*), the mean scalar profiles for various Re_* and Sc obtained from the current DNS agree well with the scaling laws given by (A 1)–(A 3) in the corresponding linear and logarithmic regions. Similarly, the profiles of $\overline{\theta'}^+_{rms}$ also agree well with the previous DNS result from Debusschere & Rutland (2004) and the linear scaling law found by Antonia & Kim (1991) and Kawamura *et al.* (1998).

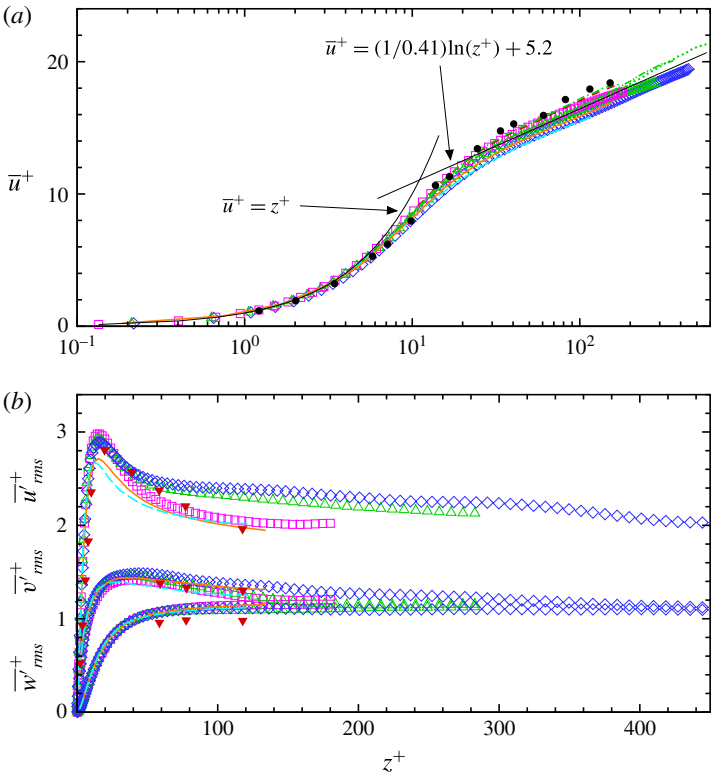

FIGURE 27. (Colour online) Profiles of (*a*) mean streamwise velocity $\overline{u}^+$ and (*b*) velocity fluctuation r.m.s. ($\overline{u'^+_{rms}}$, $\overline{v'^+_{rms}}$, $\overline{w'^+_{rms}}$) in turbulent flows over a flat boundary. Experimental data are denoted by solid symbols: ●, channel flow at $Re_* = 142$ from Eckelmann (1974) (modified by Kim *et al.* 1987); +, Couette flow at $Re_* = 82$ from Aydin & Leutheusser (1991); ×, Couette flow at $Re_* = 134$ from Aydin & Leutheusser (1991); ▼, Couette flow at $Re_* = 434$ from El Telbany & Reynolds (1982). DNS results are denoted by lines: – – –, channel flow at $Re_* = 180$ from Kim *et al.* (1987); — · —, channel flow at $Re_* = 180$ from Moser, Kim & Mansour (1999); — · · —, channel flow at $Re_* = 395$ from Moser *et al.* (1999); · · · , channel flow at $Re_* = 590$ from Moser *et al.* (1999); – –, Couette flow at $Re_* = 120$ from Sullivan *et al.* (2000); ——, Couette flow at $Re_* = 157$ from Papavassiliou & Hanratty (1997). The current DNS results of Couette flows are denoted by open symbols: □, $Re_* = 180$; △, $Re_* = 283$; ◇, $Re_* = 445$. In (*a*), the reference linear profile $\overline{u}^+ = z^+$ and logarithmic profile $\overline{u}^+ = (1/0.41)\ln(z^+) + 5.2$ are denoted by thin solid lines.

Appendix B. Averaging on ζ-plane versus on z-plane

In the triple decomposition approach used for analyzing the DNS results (see equation (4.1)), the mean velocity and scalar are calculated by averaging on the planes of constant ζ, which is defined by the grid algebraic mapping equation (2.12). As shown in figure 29(*a*), the grid lines of constant ζ are nearly parallel to the wave surface near the lower boundary of the simulation domain. Thus, computing the mean quantities along ζ-planes allows us to obtain the correct linear profiles in the thin viscous sublayer, which is within 5 wall units above the curved wave surface. Such a thin viscous sublayer cannot be captured if the average is done along z-planes, as

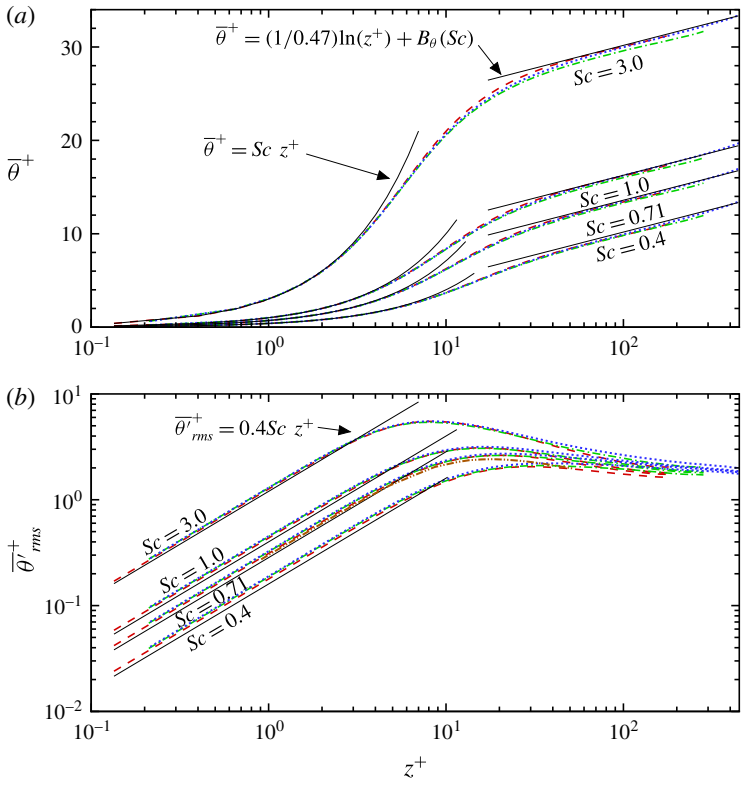

FIGURE 28. (Colour online) Profiles of (*a*) mean scalar $\overline{\theta}^+$ and (*b*) scalar fluctuation r.m.s. $\overline{\theta'}^+_{rms}$ in turbulent flows over a flat boundary. The DNS results for three different Reynolds numbers are shown: – – –, $Re_* = 180$; — · —, $Re_* = 283$; and · · · , $Re_* = 445$. For each Reynolds number, four different Schmidt numbers are shown, i.e. $Sc = 0.4$, 0.71, 1.0 and 3.0. In (*a*), the reference linear profile $\overline{\theta}^+ = Sc\, z^+$ and logarithmic profile $\overline{\theta}^+ = (1/\kappa_\theta)\ln(z^+) + B_\theta(Sc)$ suggested by Kader (1981) are denoted by thin solid lines for each Schmidt number, where $\kappa_\theta = 0.47$ and $B_\theta(Sc) = (3.84Sc^{1/3} - 1.3)^2 + 2.12\ln(Sc)$. In (*b*), the linear reference profile $\overline{\theta'}^+_{rms} = 0.4Sc\, z^+$ for each corresponding Sc is denoted by thin solid lines, and the DNS result from Debusschere & Rutland (2004) for $Re_* = 160$ and $Sc = 0.7$ is denoted by — · · —.

it does not have a valid definition in the flow regions lower than the elevation of the wave crest as shown in figure 29(*b*).

Overall, the mean profiles based on ζ-plane averaging merge to the corresponding mean profiles based on z-plane averaging because the ζ-plane becomes flatter towards higher elevation (see the grid lines in figure 29*a*). Near the wave surface, z-plane averaging yields lower values than the ζ-plane averaging due to the wave-induced distortion. We remark that for a flat-wall turbulent boundary layer, the log-law region is typically defined to be within $30 < z^+ < 0.3\delta^+$, where δ^+ is the half-domain height in wall units (see table 7.1 in Pope 2000). Note that the wave crest in the current study has a height of $\eta^+_{crest} = 17.7$ and the averaged half-domain height is $\delta^+ = 445$, therefore the log-law region in the current DNS should be defined as $50 < z^+ < 150$ considering the additional vertical displacement of the mean profile by the wave crest.

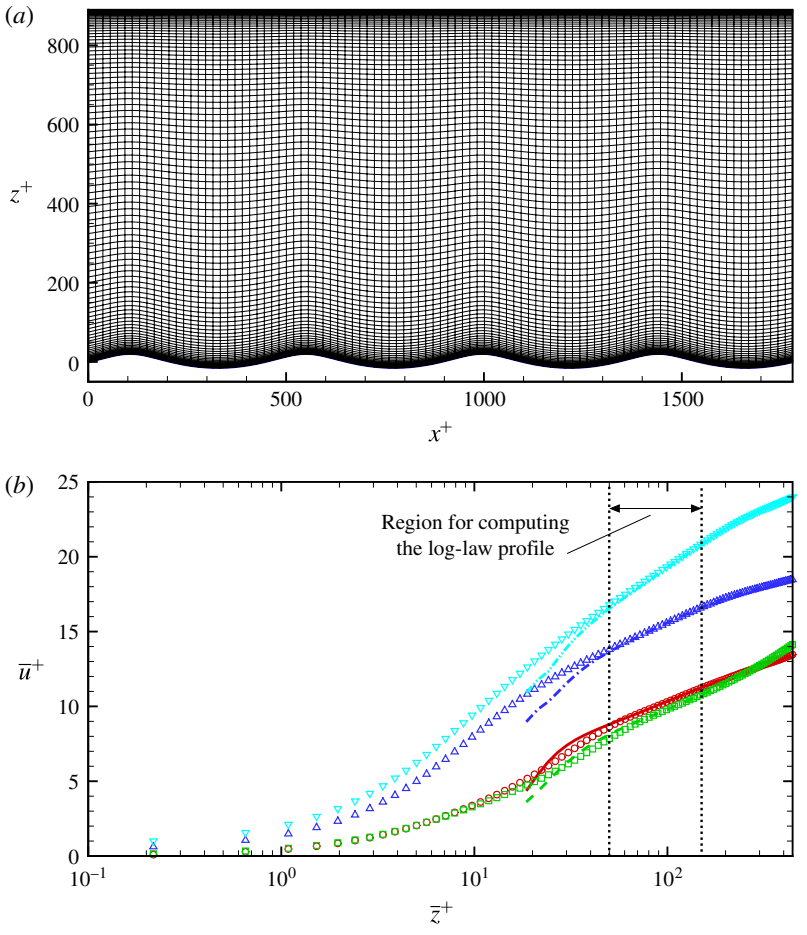

FIGURE 29. (Colour online) Comparison of ζ-plane averaging with z-plane averaging. Panel (a) shows the boundary-fitted computational grid used in the current DNS, with each of the horizontal grid lines corresponding to a constant ζ in the computational space (ξ, ψ, ζ, τ). For illustration purposes, the grid lines on a (x, z)-plane are plotted for every two actual grids used in the simulation. Panel (b) shows the comparison of the mean streamwise velocity $\overline{u}^+$ obtained by averaging on planes of constant ζ (open symbols) versus on planes of constant z (lines): ○ and ——, S25 $(c/u_* = 0)$; □ and − − −, W25C2 $(c/u_* = 2)$; △ and — · —, W25C14 $(c/u_* = 14)$; ▽ and — · · —, W25C25 $(c/u_* = 25)$. When evaluating the log-law profile, the mean velocity within $50 < z^+ < 150$ is used, as marked by the two dotted lines.

Figure 29(b) shows that the mean profiles obtained by ζ-plane averaging and z-plane averaging agree very well in the log-law region. The above analyses show that it is an appropriate choice to compute the mean quantities based on the ζ-plane averaging for the statistical analyses performed in this study.

Appendix C. Conditional average based on quadrants of scalar flux

The vertical turbulent flux of the scalar, $\langle -\theta' w' \rangle$, can be decomposed into four parts based on the quadrants in the (θ', w') space: Q1 $(\theta' > 0, w' > 0)$, Q2 $(\theta' < 0, w' > 0)$,

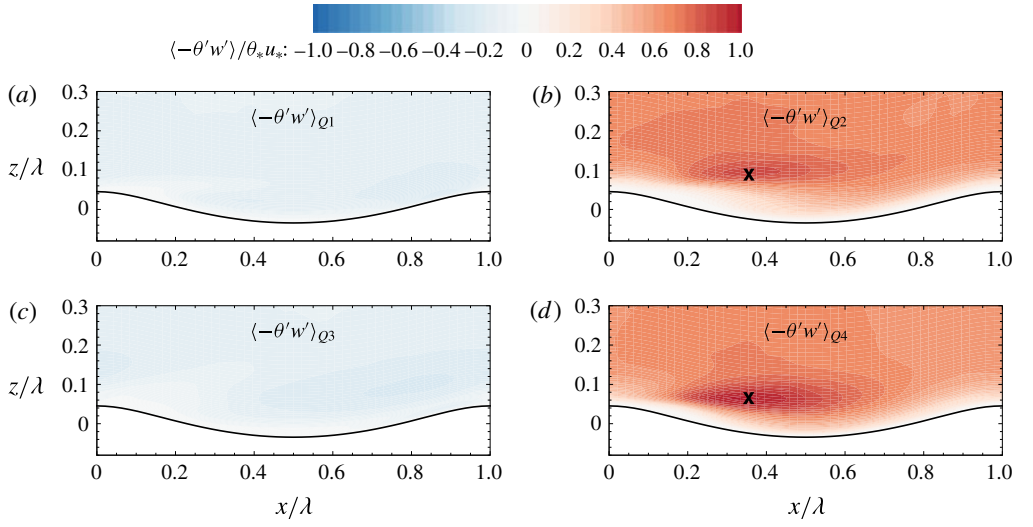

FIGURE 30. (Colour online) Decomposed vertical scalar flux $\langle -\theta' w' \rangle$ for case W25C2 with $Sc = 1.0$ based on the four quadrants: (*a*) Q1 ($\theta' > 0, w' > 0$); (*b*) Q2 ($\theta' < 0, w' > 0$); (*c*) Q3 ($\theta' < 0, w' < 0$); and (*d*) Q4 ($\theta' > 0, w' < 0$). In (*b*) and (*d*), each of the corresponding detection position for quadrant-based conditional sampling is chosen to be the grid point at the maximum of the corresponding quadrant and is marked by the cross symbol. In case W25C2, the Q1 and Q3 events contribute very little to $\langle -\theta' w' \rangle$, thus are not considered in the quadrant-based conditional sampling analysis.

Q3 ($\theta' < 0, w' < 0$) and Q4 ($\theta' > 0, w' < 0$). Figures 30 and 31 show the decomposed turbulent scalar flux $\langle -\theta' w' \rangle$ for cases W25C2 and W25C14, respectively. In case W25C2, quadrants Q2 and Q4 make the greatest contributions to the total flux, while the contributions from Q1 and Q3 are significantly smaller. In case W25C14, the four quadrants make comparable contributions to the total flux, with Q1 and Q3 for the negative flux region above the windward face and Q2 and Q4 for the positive flux region above the leeward face. The results for case W25C25 are very similar to those in case W25C14, and are thus not shown here due to space limitations.

For the quadrant-based conditional average shown in § 4.6, samples are taken from the instantaneous snapshots of the velocity and scalar fields using the quadrant events detector (Kim & Moin 1986; Yang & Shen 2009),

$$D_i(y, t; x_s, z_s) = \begin{cases} 1, & \text{if } (\theta', w') \in \mathrm{Q}i \text{ and } \dfrac{-\theta' w'}{\langle -\theta' w' \rangle} > 2, \\ 0, & \text{otherwise.} \end{cases} \tag{C 1}$$

This detection function is applied to a number of instantaneous snapshots at different time t. Samples for quadrant Qi are taken if $D_i(y, t; x_s, z_s) = 1$. Moreover, the detection function scans over all the y for each snapshot, but uses fixed values for (x_s, z_s) for each quadrant event so that samples are taken at a consistent location relative to the wave phase. The (x_s, z_s) location for each quadrant is chosen to be the grid point that has the maximum of the contribution to $\langle -\theta' w' \rangle$ due to the corresponding quadrant, and the specific locations for cases W25C2 and W25C14 are marked in figures 30 and 31, respectively. For each case, 400 instantaneous snapshots of the

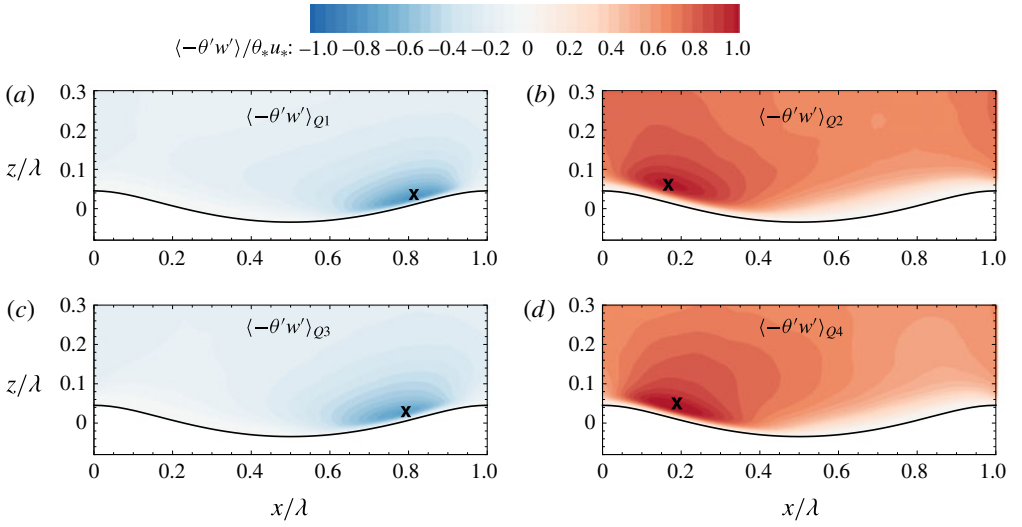

FIGURE 31. (Colour online) Decomposed vertical scalar flux $\langle -\theta' w' \rangle$ for case W25C14 with $Sc = 1.0$ based on the four quadrants: (*a*) Q1 ($\theta' > 0, w' > 0$); (*b*) Q2 ($\theta' < 0, w' > 0$); (*c*) Q3 ($\theta' < 0, w' < 0$); and (*d*) Q4 ($\theta' > 0, w' < 0$). In each panel, the corresponding detection position for quadrant-based conditional sampling is chosen to be the grid point at the maximum of the corresponding quadrant and is marked by the cross symbol.

full three-dimensional velocity and scalar fields are used for conditional average, with each snapshot consisting of four wavelengths. For the analysis reported in this paper, in (C 1) the samples are high-pass filtered by the criterion $-\theta' w' / \langle -\theta' w' \rangle > 2$, i.e. samples are taken only when the magnitude of the detected instantaneous vertical flux is at least twice of the phase-averaged flux at the detection location. In addition to the threshold of 2, other values have also been tested for the high-pass filter criterion (e.g. 0.5, 1, 4 and 8), but insignificant differences were found in the educed flow and scalar fields, suggesting that the conditional average criterion used in the present analysis is representative.

REFERENCES

ANDERSON, D. A., TANNEHILL, J. C. & PLETCHER, R. H. 1984 *Computational Fluid Mechanics and Heat Transfer*. McGraw Hill.

ANTONIA, R. A. & KIM, J. 1991 Turbulent Prandtl number in the near-wall region of a turbulent channel flow. *Intl J. Heat Mass Transfer* **34**, 1905–1908.

AYDIN, E. M. & LEUTHEUSSER, H. J. 1991 Plane-Couette flow between smooth and rough walls. *Exp. Fluids* **11**, 302–312.

BANNER, M. L. & MELVILLE, W. K. 1976 On the separation of air flow over water waves. *J. Fluid Mech.* **77**, 825–842.

BELCHER, S. E. & HUNT, J. C. R. 1998 Turbulent flow over hills and waves. *Annu. Rev. Fluid Mech.* **30**, 507–538.

BOURASSA, M. A., VINCENT, D. G. & WOOD, W. L. 1999 A flux parameterization including the effects of capillary waves and sea state. *J. Atmos. Sci.* **56**, 1123–1139.

BUCKLEY, M. P. & VERON, F. 2016 Structure of the airflow above surface waves. *J. Phys. Oceanogr.* **46**, 1377–1397.

CHARNOCK, H. 1955 Wind stress on a water surface. *Q. J. R. Meteorol. Soc.* **81**, 639–640.

CHOI, H. S. & SUZUKI, K. 2005 Large eddy simulation of turbulent flow and heat transfer in a channel with one wavy wall. *Intl J. Heat Fluid Flow* **26**, 681–694.

CRAFT, T. J. & LAUNDER, B. E. 1996 A Reynolds stress closure designed for complex geometries. *Intl J. Heat Fluid Flow* **17**, 245–254.

DE ANGELIS, V., LOMBARDI, P. & BANERJEE, S. 1997 Direct numerical simulation of turbulent flow over a wavy wall. *Phys. Fluids* **9**, 2429–2442.

DEAN, R. G. & DALRYMPLE, R. A. 1991 *Water Wave Mechanics for Engineers and Scientists*. World Scientific.

DEBUSSCHERE, B. & RUTLAND, C. J. 2004 Turbulent scalar transport mechanisms in plane channel and Couette flows. *Intl. J. Heat Mass Transfer* **47**, 1771–1781.

DECOSMO, J., KATSAROS, K. B., SMITH, S. D., ANDERSON, R. J., OOST, W. A., BUMKE, K. & CHADWICK, H. 1996 Air–sea exchange of water vapor and sensible heat: the humidity exchange of the sea experiment (HEXOS) results. *J. Geophys. Res.* **101** (C5), 12001–12016.

DELLIL, A. Z., AZZI, A. & JUBRAN, B. A. 2004 Turbulent flow and convective heat transfer in a wavy wall channel. *Heat Mass Transfer* **40**, 793–799.

DOMMERMUTH, D. G. & YUE, D. K. P. 1987 A high-order spectral method for the study of nonlinear gravity waves. *J. Fluid Mech.* **184**, 267–288.

DONELAN, M. A. 1990 Air-sea interaction. In *The Sea* (ed. B. LeMehaute & D. M. Hanes), vol. 9, pp. 239–292. Wiley-Interscience.

DONELAN, M. A., BABANIN, A. V., YOUNG, I. R. & BANNER, M. L. 2006 Wave-follower field measurements of the wind-input spectral function. Part II. Parameterization of the wind input. *J. Phys. Oceanogr.* **36**, 1672–1689.

DRUZHININ, O. A., TROITSKAYA, Y. I. & ZILITINKEVICH, S. S. 2012 Direct numerical simulation of a turbulent wind over a wavy water surface. *J. Geophys. Res.* **117**, C00J05.

DRUZHININ, O. A., TROITSKAYAA, Y. I. & ZILITINKEVICH, S. S. 2016 Stably stratified airflow over a waved water surface. Part 1: stationary turbulence regime. *Q. J. R. Meteorol. Soc.* **142**, 759–772.

ECKELMANN, H. 1974 The structure of the viscous sublayer and the adjacent wall region in a turbulent channel flow. *J. Fluid Mech.* **65**, 439–459.

EDSON, J., CRAWFORD, T., CRESCENTI, J., FARRAR, T., FREW, N., GERBI, G., HELMIS, C., HRISTOV, T., KHELIF, D., JESSUP, A. *et al.* 2007 The coupled boundary layers and air-sea transfer experiment in low winds. *Bull. Am. Meteorol. Soc.* **88**, 342–356.

EDSON, J. B., ZAPPA, C. J., WARE, J. A., MCGILLIS, W. R. & HARE, J. E. 2004 Scalar flux profile relationships over the open ocean. *J. Geophys. Res.* **109**, C08S09.

EL TELBANY, M. M. M. & REYNOLDS, A. J. 1982 The structure of turbulent plane Couette. *Trans. ASME J. Fluids Engng* **104**, 367–372.

FAIRALL, C. W., BRADLEY, E. F., ROGERS, D. P., EDSON, J. B. & YOUNG, G. S. 1996 Bulk parameterization of air-sea fluxes for tropical ocean-global atmosphere coupled-ocean atmosphere response experiment. *J. Geophys. Res.* **101**, 3747–3764.

GENT, P. R. & TAYLOR, P. A. 1976 A numerical model of the air flow above water waves. *J. Fluid Mech.* **77**, 105–128.

GENT, P. R. & TAYLOR, P. A. 1977 A note on 'separation' over short wind waves. *Boundary-Layer Meteorol.* **11**, 65–87.

HARA, T. & SULLIVAN, P. P. 2015 Wave boundary layer turbulence over surface waves in a strongly forced condition. *J. Phys. Oceanogr.* **45**, 868–883.

HASEGAWA, Y. & KASAGI, N. 2008 Systematic analysis of high Schmidt number turbulent mass transfer across clean, contaminated and solid interfaces. *Intl J. Heat Fluid Flow* **29**, 765–773.

HOYAS, S. & JIMÉNEZ, J. 2006 Scaling of the velocity fluctuations in turbulent channels up to $Re_\tau = 2003$. *Phys. Fluids* **18**, 011702.

HRISTOV, T. S., MILLER, S. D. & FRIEHE, C. A. 2003 Dynamical coupling of wind and ocean waves through wave-induced air flow. *Nature* **422**, 55–58.

JÄHNE, B. & HAUßECKER, H. 1998 Air–water gas exchange. *Annu. Rev. Fluid Mech.* **30**, 443–468.

JEONG, J. & HUSSAIN, F. 1995 On the identification of a vortex. *J. Fluid Mech.* **285**, 69–94.

JOHNSON, H. K., HØSTRUP, J., VESTED, H. J. & LARSEN, S. E. 1998 On the dependence of sea surface roughness on wind waves. *J. Phys. Oceanogr.* **28**, 1702–1716.

KADER, B. A. 1981 Temperature and concentration profiles in fully turbulent boundary layers. *Intl J. Heat Mass Transfer* **24**, 1541–1544.

KATSOUVAS, G. D., HELMIS, C. G. & WANG, Q. 2007 Quadrant analysis of the scalar and momentum fluxes in the stable marine atmospheric surface layer. *Boundary-Layer Meteorol.* **124**, 335–360.

KATUL, G. G., SEMPREVIVA, A. M. & CAVA, D. 2008 The temperature–humidity covariance in the marine surface layer: a one-dimensional analytical model. *Boundary-Layer Meteorol.* **126**, 263–278.

KAWAMURA, H., OHSAKA, K., ABE, H. & YAMAMOTO, K. 1998 DNS of turbulent heat transfer in channel flow with low to medium-high Prandtl number fluid. *Intl J. Heat Fluid Flow* **19**, 482–491.

KIHARA, N., HANAZAKI, H., MIZUYA, T. & UEDA, H. 2007 Relationship between airflow at the critical height and momentum transfer to the traveling waves. *Phys. Fluids* **19**, 015102.

KIM, J. & MOIN, P 1986 The structure of the vorticity field in turbulent channel flow. Part 2. Study of ensemble-averaged fields. *J. Fluid Mech.* **162**, 339–363.

KIM, J. & MOIN, P. 1989 Transport of passive scalars in a turbulent channel flow. In *Turbulent Shear Flows 6* (ed. J.-C. André, J. Cousteix, F. Durst, B. E. Launder, F. W. Schmidt & J. H. Whitelaw), pp. 85–96. Springer.

KIM, J., MOIN, P. & MOSER, R. 1987 Turbulence statistics in fully developed channel flow at low Reynolds number. *J. Fluid Mech.* **177**, 133–166.

KITAIGORODSKII, S. A. & DONELAN, M. A. 1984 Wind–wave effects on gas transfer. In *Gas Transfer at Water Surfaces* (ed. W. Brutsaert & G. H. Jirka). Reidel.

LEE, M. & MOSER, R. D. 2015 Direct numerical simulation of turbulent channel flow up to $Re_\tau \approx 5200$. *J. Fluid Mech.* **774**, 416–442.

LI, P. Y., XU, D. & TAYLOR, P. A. 2000 Numerical modeling of turbulent airflow over water waves. *Boundary-Layer Meteorol.* **95**, 397–425.

LIGHTHILL, M. J. 1962 Physical interpretation of the mathematical theory of wave generation by wind. *J. Fluid Mech.* **14**, 385–398.

MEIRINK, J. F. & MAKIN, V. K. 2000 Modelling low-Reynolds-number effects in the turbulent air flow over water waves. *J. Fluid Mech.* **415**, 155–174.

MILES, J. W. 1957 On the generation of surface waves by shear flows. *J. Fluid Mech.* **3**, 185–204.

MOSER, R. D., KIM, J. & MANSOUR, N. N. 1999 Direct numerical simulation of turbulent channel flow up to $Re_\tau = 590$. *Phys. Fluids* **11**, 943–945.

NA, Y., PAPAVASSILIOU, D. V. & HANRATTY, T. J. 1999 Use of direct numerical simulation to study the effect of Prandtl number on temperature fields. *Intl J. Heat Fluid Flow* **20**, 187–195.

PAPAVASSILIOU, D. V. & HANRATTY, T. J. 1997 Interpretation of large-scale structures observed in a turbulent plane Couette flow. *Intl J. Heat Fluid Flow* **18**, 55–69.

PARK, T. S., CHOI, H. S. & SUZUKI, K. 2004 Nonlinear k–ϵ–f_μ model and its application to the flow and heat transfer in a channel having one undulant wall. *Intl J. Heat Mass Transfer* **47**, 2403–2415.

POPE, S. B. 2000 *Turbulent Flows*. Cambridge University Press.

ROBINSON, S. K. 1991 Coherent motions in the turbulent boundary layer. *Annu. Rev. Fluid Mech.* **23**, 601–639.

ROSSI, R. 2010 A numerical study of algebraic flux models for heat and mass transport simulation in complex flows. *Intl J. Heat Mass Transfer* **53**, 4511–4524.

RUTGERSSON, A. & SULLIVAN, P. P. 2005 The effect of idealized water waves onthe turbulence structure and kinetic energy budgets in the overlying airflow. *Dyn. Atmos. Ocean* **38**, 147–171.

SCHWARTZ, L. W. 1974 Computer extension and analytic continuation of Stokes' expansion for gravity waves. *J. Fluid Mech.* **62**, 553–578.

SHAW, D. A. & HANRATTY, T. J. 1977 Turbulent mass transfer to a wall for large Schmidt numbers. *AIChE J.* **23**, 28–37.

SMITH, S. D. 1988 Coefficients for sea surface wind stress, heat flux and wind profiles as a function of wind speed and temperature. *J. Geophys. Res.* **93**, 15467–15472.

STEWART, R. H. 1970 Laboratory studies of the velocity field over deep-water waves. *J. Fluid Mech.* **42**, 733–754.

STOKES, G. G. 1847 On the theory of oscillatory waves. *Trans. Camb. Phil. Soc.* **8**, 441–455.

SULLIVAN, P. P., EDSON, J. B., HRISTOV, T. S. & MCWILLIAMS, J. C. 2008 Large-eddy simulations and observations of atmospheric marine boundary layers above nonequilibrium surface waves. *J. Atmos. Sci.* **65**, 1225–1245.

SULLIVAN, P. P. & MCWILLIAMS, J. C. 2002 Turbulent flow over water waves in the presence of stratification. *Phys. Fluids* **14**, 1182–1194.

SULLIVAN, P. P. & MCWILLIAMS, J. C. 2010 Dynamics of winds and currents coupled to surface waves. *Annu. Rev. Fluid Mech.* **42**, 19–42.

SULLIVAN, P. P., MCWILLIAMS, J. C. & MOENG, C.-H. 2000 Simulation of turbulent flow over idealized water waves. *J. Fluid Mech.* **404**, 47–85.

TOBA, Y., SMITH, S. D. & EBUCHI, N. 2001 Historical drag expressions. In *Wind Stress over the Ocean*. (ed. I. S. F. Jones & Y. Toba), pp. 35–53. Cambridge University Press.

TSENG, Y.-H. & FERZIGER, J. H. 2003 A ghost-cell immersed boundary method for flow in complex geometry. *J. Comput. Phys.* **192**, 593–623.

VINOKUR, M. 1974 Conservation equations of gas-dynamics in curvilinear coordinate systems. *J. Comput. Phys.* **14**, 105–125.

WALLACE, J. M. 2016 Quadrant analysis in turbulence reserach: history and evolution. *Annu. Rev. Fluid Mech.* **48**, 131–158.

YANG, D., MENEVEAU, C. & SHEN, L. 2013 Dynamic modelling of sea-surface roughness for large-eddy simulation of wind over ocean wavefield. *J. Fluid Mech.* **726**, 62–99.

YANG, D., MENEVEAU, C. & SHEN, L. 2014*a* Effect of downwind swells on offshore wind energy harvesting – a large-eddy simulation study. *J. Renew. Energy* **70**, 11–23.

YANG, D., MENEVEAU, C. & SHEN, L. 2014*b* Large-eddy simulation of offshore wind farm. *Phys. Fluids* **26**, 025101.

YANG, D. & SHEN, L. 2009 Characteristics of coherent vortical structures in turbulent flows over progressive surface waves. *Phys. Fluids* **21**, 125106.

YANG, D. & SHEN, L. 2010 Direct-simulation-based study of turbulent flow over various waving boundaries. *J. Fluid Mech.* **650**, 131–180.

YANG, D. & SHEN, L. 2011*a* Simulation of viscous flows with undulatory boundaries. Part I: basic solver. *J. Comput. Phys.* **230**, 5488–5509.

YANG, D. & SHEN, L. 2011*b* Simulation of viscous flows with undulatory boundaries. Part II: coupling with other solvers for two-fluid computations. *J. Comput. Phys.* **230**, 5510–5531.

YANG, J. & BALARAS, E. 2006 An embedded-boundary formulation for large-eddy simulation of turbulent flows interacting with moving boundaries. *J. Comput. Phys.* **215**, 12–40.

ZANG, Y., STREET, R. L. & KOSEFF, J. R. 1994 A non-staggered grid, fractional step method for time-dependent incompressible Navier–Stokes equations in curvilinear coordinates. *J. Comput. Phys.* **114**, 18–33.

ZEDLER, E. A. & STREET, R. L. 2001 Large-eddy simulation of sediment transport: currents over ripples. *ASCE J. Hydraul. Engng* **127**, 444–452.